



Improvement of Imaging Conditions to Improve the Detection Rate of Head and Neck Cancer by Positron Emission Tomography/Computed Tomography Examination

Hayato Odagiri,^{1,2} Kentaro Takanami,² Tomohiro Kaneta,^{1,2} Akihito Usui,¹ Ikuho Kojima,³ Hiroyasu Kodama,⁴ Shin Saitou,⁴ Yoshitaka Tanaka,⁴ Yutaka Dendo⁴ and Kei Takase²

¹Department of Diagnostic Image Analysis, Tohoku University Graduate School of Medicine, Sendai, Miyagi, Japan

²Department of Diagnostic Radiology, Tohoku University Hospital, Sendai, Miyagi, Japan

³Department of Oral and Maxillofacial Radiology, Tohoku University Hospital, Sendai, Miyagi, Japan

⁴Department of Radiology, Tohoku University Hospital, Sendai, Miyagi, Japan

Positron emission tomography (PET)/computed tomography (CT) has improved sensitivity and resolution using silicon photomultiplier as a photosensor. Previously, only a fixed setting was available for the shooting time of 1 bed, but now, the shooting time can be changed for each bed. Time can be shortened or extended depending on the target area. A few studies reported on image reconstruction conditions for head and neck cancer in whole-body PET/CT examinations. Thus, this study aimed to optimize the imaging conditions of the head and neck region during whole-body imaging. A cylindrical acrylic container with a 200 mm diameter was used to simulate the head and neck area using a PET/CT system equipped with a semiconductor detector. Spheres of 6-30 mm in diameter were enclosed in the 200 mm diameter cylindrical acrylic vessel. Radioactivity in ¹⁸F solution (Hot:BG ratio 4:1) was enclosed in a phantom following the Japanese Society of Nuclear Medicine (JSNM) guidelines. Background radioactivity concentration was 2.53 kBq/mL. List mode acquisition of 1,800 s was collected at 60-1,800 s with the field of view of 700 mm and 350 mm. The image was reconstructed by resizing the matrix to 128 × 128, 192 × 192, 256 × 256, and 384 × 384, respectively. The imaging time per bed in the head and neck should be at least 180 s, and the reconstruction conditions should be a field of view (FOV) of 350 mm, matrix sizes of ≥ 192, and a Bayesian penalized likelihood (BPL) reconstruction with a β -value of 200. This allows detection of > 70% of the 8-mm spheres in the images.

Keywords: BPL reconstruction; head and neck cancer; PET/CT system; reconstruction parameters; recovery coefficient

Tohoku J. Exp. Med., 2023 June, 260 (2), 141-147.

doi: 10.1620/tjem.2023.J026

Introduction

The positron emission tomography (PET) using 2-Deoxy-2-[fluoro-¹⁸F] fluoro-d-glucose (¹⁸F-FDG) is a very useful tool for determining lesion extent and therapeutic efficacy in patients with cancer (Beyer et al. 2000; Fletcher et al. 2008). PET/computed tomography (CT) system have improved sensitivity using semiconductor elements in the detector in recent years, as well as improved resolution due

to new correction techniques (Chicheportiche et al. 2020). Previously, the PET scan time for one bed position was fixed; however, now, that can be changed for each bed position. For example, when incorporating respiratory synchronization for a patient with lung cancer, scan time can be extended for the lung and shortened for the lower extremities. Generally, a PET scan for a patient with cancer is performed for 90-180 s per bed position, based on the vendor's recommendation. This is based on the results of phantom

Received January 16, 2023; revised and accepted March 20, 2023; J-STAGE Advance online publication March 30, 2023

Correspondence: Hayato Odagiri, Department of Diagnostic Image Analysis, Tohoku University Graduate School of Medicine, 2-1 Seiryomachi, Aoba-ku, Sendai, Miyagi 980-8575, Japan.

e-mail: hayato.odagiri.e2@tohoku.ac.jp

©2023 Tohoku University Medical Press. This is an open-access article distributed under the terms of the Creative Commons Attribution-NonCommercial-NoDerivatives 4.0 International License (CC-BY-NC-ND 4.0). Anyone may download, reuse, copy, reprint, or distribute the article without modifications or adaptations for non-profit purposes if they cite the original authors and source properly.

<https://creativecommons.org/licenses/by-nc-nd/4.0/>

experiments conducted at various facilities following their guidelines (Fukukita et al. 2014). However, the phantoms used in the guideline were designed for the torso, not for the head or neck. In addition, whole-body PET images are reconstructed with a field of view (FOV) of approximately 700 mm; however, this size appears to be too big for the head and neck region. PET images of head and neck cancer are expected to provide precise detection of small primary or metastatic lesions for evaluating treatment response to therapy and as surveillance for recurrence (Schöder et al. 2004; Wang et al. 2006). Few reports have examined the optimal imaging and reconstruction conditions for evaluating neck lesions in whole-body imaging although studies of image reconstruction conditions were conducted to evaluate the brain (Lindström et al. 2020; Wagatsuma et al. 2020; Ishii et al. 2023). In this study, we performed experiments using a new smaller phantom that appeared to be appropriate for the head and neck region compared with the standard National Electrical Manufacturers Association body phantom. This study aimed to clarify the optimal imaging time and reconstruction conditions for the head and neck region using this phantom.

Materials and Methods

Cylindrical phantom

The ECT Hot Cold Phantom SP-6 (Kyoto Kagaku Co., Ltd., Kyoto, Japan) in spheres of 30 mm, 20 mm, 10 mm, 8 mm, and 6 mm in diameter were placed in a cylindrical acrylic container of 200 mm in diameter, assuming a tumor, and adjusted so that the radioactivity concentration was four times the sphere concentration relative to background 1. The radioactivity concentration of 2.53 kBq/mL in the background region was assumed as the radioactivity concentration in soft tissues imaged by PET after a standard dose of 3.7 MBq/kg for 1 h as indicated in the ^{18}F -FDG-PET cancer screening guidelines (Fukukita et al. 2014).

PET/CT systems and reconstruction parameters

Scan was performed using a Discovery MI (GE Healthcare, Milwaukee, WI, USA) PET/CT system. This system consists of the 4-ring detector block coupled with an array of lutetium yttrium orthosilicate crystals and silicon photomultiplier (SiPM) as a photosensor and a 64-slice CT scanner. The PET detector has a transaxial field of view of 700 mm and an axial field of view of 200 mm with a 24% overlap between bed positions. The sensitivity based on the National Electrical Manufacturers Association (NEMA) NU 2-2012 standard was 13.5 cps/kBq (Chicheportiche et al. 2020). CT imaging for attenuation correction was performed, followed by PET imaging. The scan was taken in the list mode for 1,800 s to obtain sufficient counting statistics.

Image analysis

Reconstruction was performed using the Bayesian penalized likelihood (BPL) reconstruction algorithm incor-

porating a noise-suppressing penalization factor (β -value). Time of flight and point spread function were included for resolution recovery (Teoh et al. 2015; Kurita et al. 2020). Data collected in the 1,800 s list mode were taken by changing the acquisition time to 60, 120, 180, 240, 300, 600, 900, and 1,800 s, and the effective field of view (FOV) of 350 mm, matrix size 128×128 , 192×192 , 256×256 , and 384×384 . Image reconstruction was performed using the BPL reconstruction with β -values of 600 and 200. The comparison was made with the quantitative values when the torso was reconstructed with a FOV of 700 mm, a matrix size of 192×192 , and a β -value of 600. Pixel size for a FOV of 700 mm and matrix size of 192×192 was 3.64 mm, and for a FOV of 350 mm and matrix sizes of 128×128 , 192×192 , 256×256 , and 384×384 are 2.73 mm, 1.82 mm, 1.37 mm, and 0.91 mm, respectively. Image analysis was performed using RAVAT (Nihon Medi-Physics Co., Ltd., Tokyo, Japan), with the region of interest (ROI) of the same size as each hot sphere, and the maximum standardized uptake value (SUV_{max}) was calculated (Daisaki et al. 2021; Tateishi et al. 2021).

Recovery coefficient (RC)

The SUV_{max} was measured by focusing on the slice with the widest sphere in the PET image from the data collected during the 1,800 s imaging time and using that sphere as the ROI. The relative RC for each sphere was calculated using the SUV_{max} of the 30-mm sphere as a reference. Three sets of 120 s data were generated for the RC, and the mean and standard deviation for each sphere were calculated. A relative RC graph for each reconstructed condition was created from the obtained RC. Statistical analysis was performed with JMP Pro, version 16 (SAS Institute Inc., Cary, NC, USA) using Student's t-test. p-value < 0.05 was considered a significant difference.

$$\text{RC}_j = \frac{\text{SUV}_{\text{max},j}}{\text{SUV}_{\text{max},30 \text{ mm}}}$$

Background variability evaluation

Twelve 30 mm circular ROIs were placed in the widest spherical center slice and on ± 1 and ± 2 cm away from the central slice of the PET image, for a total of 60 interest regions ($k = 60$) for background measurement in 5 slices, and $C_{\text{B},30 \text{ mm}}$ of the average count was calculated. The percent background variability $N_{30 \text{ mm}}$ for the 30-mm sphere is calculated as follows:

$$N_{30 \text{ mm}} = \frac{\text{SD}_{30 \text{ mm}}}{C_{\text{B},30 \text{ mm}}} \times 100$$

$\text{SD}_{30 \text{ mm}}$ is the standard deviation of the background ROI counts for the 30-mm sphere, which is calculated as follows:

$$\text{SD}_{30 \text{ mm}} = \sqrt{\frac{\sum_{k=1}^K (C_{\text{B},30 \text{ mm},k} - C_{\text{B},30 \text{ mm}})^2}{k-1}}$$

Contrast evaluation

Twelve ROIs of the same size are drawn on slices as close as possible on both sides ± 1 cm and ± 2 cm from the central slice, for a total of 60 background ROIs (on 5 slices 12 on each). The positions of all ROIs are fixed between successive measurements. The activity measured in each background ROI was recorded. The percent contrast of the 30 mm thermosphere (Q_j) was calculated as follows:

$$Q_j = \frac{C_{H,j} / C_{B,30\text{mm}} - 1}{a_H / a_B - 1} \times 100$$

Where $C_{H,j}$ and $C_{B,30\text{mm}}$ are the average measured radioactivity in the ROI of the 30-mm sphere and the average measured activity in all the background 30 mm diameter ROIs, respectively. a_H and a_B were the activity concentration ratio for the hot sphere to the background.

Results

CT and PET images of the ECT hot cold phantom SP-6 were shown (Fig. 1). Even the 8 mm sphere was visible in the 1,800 s PET image with a FOV of 700 mm, matrix size of 192×192 , and a BPL reconstruction with β -values of 600, which were the clinically used image reconstruction conditions in the whole-body scan. Additionally, the 8 mm sphere was difficult to identify in the 120 s PET image with a penalty function value of

β -values of 600, but was able to be identified with β -values of 200. The phantom SP-6 PET images with a FOV of 350 mm and the BPL reconstruction with β -values of 200 were presented with different matrix sizes and scanning times (Fig. 2). Matrix sizes of 128×128 , 192×192 , 256×256 , and 384×384 have pixel sizes of 2.73 mm, 1.82 mm, 1.37 mm, 0.91 mm, respectively, but with no significant visual change. Additionally, the images with a matrix size of 192×192 and an acquisition time of 60, 120, 180, 240, 300, 600, 900, and 1,800 s show a reduction in variation of background level.

Recovery coefficient

The RC curves for different FOV and BPL reconstruction conditions are shown (Fig. 3), showing that although the effect of different FOV is small, the BPL reconstruction conditions have a significant impact on RC. Using a β -value of 200 improved RC by $> 20\%$ for 8- and 10-mm spheres compared with using a β -value of 600. Compared with an FOV of 700 mm, an FOV of 350 mm resulted in an RC of 60% for the 8-mm sphere, with less variation because of different matrix sizes. The differences in RC for different FOV and matrix sizes are shown in Table 1. The matrix sizes of 128×128 showed lower values at an FOV of 700 mm for 8- and 10-mm spheres. For matrix sizes of 192×192 and above, the effect of different FOV sizes was smaller. The RCs for different β -values in the BPL reconstruction condition for FOV of 350 mm are shown in Table

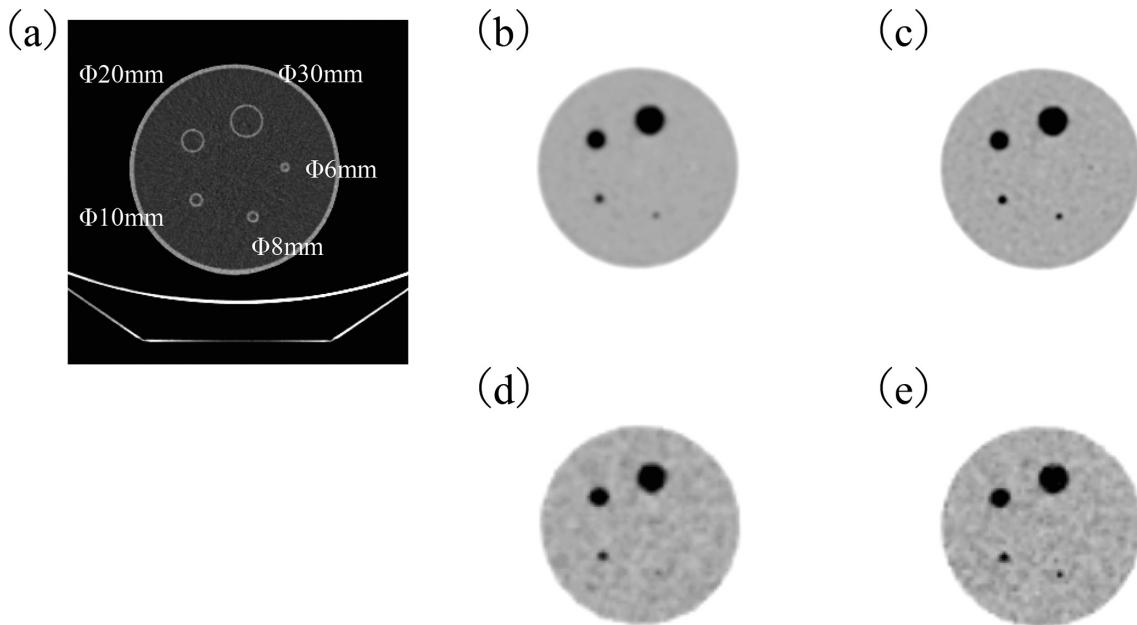


Fig. 1. Computed tomography (CT) and positron emission tomography (PET) images of ECT hot cold phantom SP-6. Images with different scanning times and Bayesian penalized likelihood reconstruction method conditions with a matrix size of 192×192 and a field of view of 700 mm.
 (a) Axial CT image and sphere size
 (b) Scanning time of 30 minutes, PET image (penalty function value of a β -value of 600)
 (c) Scanning time of 30 minutes, PET image (penalty function value of a β -value of 200)
 (d) Scanning time of 2 minutes, PET image (penalty function value of a β -value of 600)
 (e) Scanning time of 2 minutes, PET image (penalty function value of a β -value of 200)

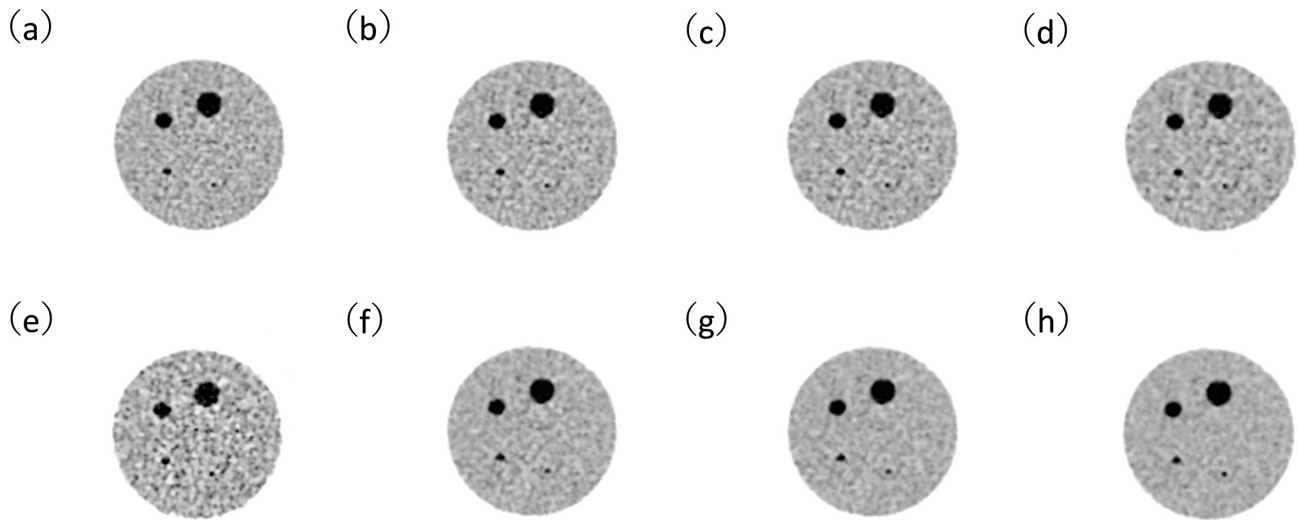


Fig. 2. Positron emission tomography images of ECT hot-cold phantom SP-6 with a field of view of 350 mm and Bayesian penalized likelihood reconstruction method conditions of a β -value of 200 with different matrix sizes and scanning times.

The scanning time was 120 s for (a) to (d), and the matrix size was 192×192 for (e) to (h). (a) Matrix size, 384×384 , (b) Matrix size, 256×256 , (c) Matrix size, 192×192 , (d) Matrix size, 128×128 , (e) Scanning time, 60 s, (f) Scanning time, 180 s, (g) Scanning time, 240 s, (h) Scanning time, 300 s.

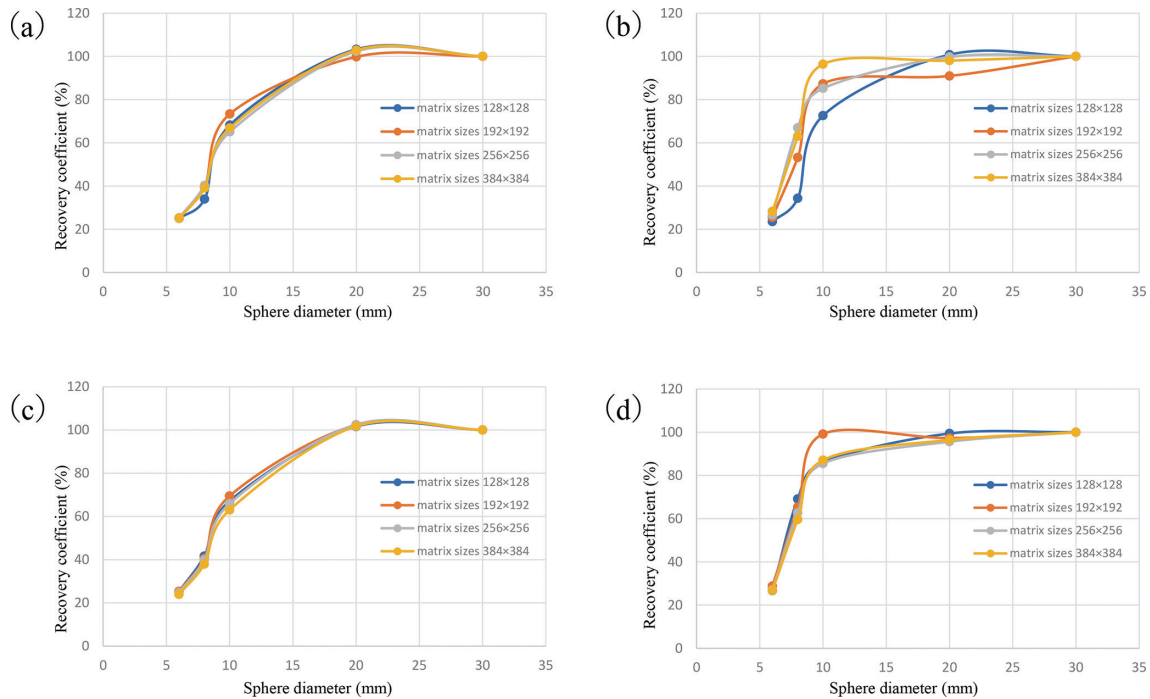


Fig. 3. The recovery coefficients were for each matrix size and Bayesian penalized likelihood reconstruction method condition.

(a) Scanning time, 2 min; field of view (FOV), 700 mm; β -value, 600, (b) Scanning time, 2 min; FOV, 700 mm; β -value, 200, (c) Scanning time, 2 min; FOV, 350 mm; β -value, 600, (d) Scanning time, 2 min; FOV, 350 mm; β -value, 200.

2. Using a β -value of 200 was significantly higher for all spheres > 8 -mm than using a β value of 600.

Background variability evaluation

Images were reconstructed at different imaging times and matrix sizes with a FOV of 350 mm using the BPL reconstruction with a β -value of 200. The background vari-

ability ($\%N_{30\text{ mm}}$) calculated from the average of 60 ROIs of 30 mm diameter set in the background region was shown in Table 3. The fluctuations in the background variability became smaller as the acquisition time increased. The background variability tended to be larger for matrix size 128×128 and smaller for matrix size 384×384 . The effect of background variability by matrix size became smaller as

Table 1. The recovery coefficients for different fields of view and matrix sizes (acquisition time of 120 s and β -value of 200).

Matrix size	FOV	128			192			256			384		
		700 mm	350 mm	p-value									
Sphere diameter	6 mm	1.11 ± 0.17	1.29 ± 0.30	0.66	1.29 ± 0.34	1.39 ± 0.31	0.77	1.26 ± 0.27	1.34 ± 0.28	0.78	1.34 ± 0.27	1.33 ± 0.23	0.99
	8 mm	1.61 ± 0.25	3.40 ± 0.19	< 0.05	2.66 ± 0.51	3.16 ± 0.49	0.16	3.22 ± 0.19	3.11 ± 0.23	0.7	2.99 ± 0.41	2.98 ± 0.20	0.97
	10 mm	3.37 ± 0.89	4.25 ± 0.29	< 0.05	4.48 ± 0.40	4.86 ± 0.24	0.28	4.11 ± 0.22	4.26 ± 0.20	0.58	4.61 ± 0.15	4.36 ± 0.14	0.25
	20 mm	4.78 ± 0.75	4.93 ± 0.67	0.73	4.60 ± 0.16	4.76 ± 0.23	0.66	4.83 ± 0.58	4.77 ± 0.30	0.81	4.69 ± 0.20	4.83 ± 0.22	0.53
	30 mm	4.75 ± 0.44	4.96 ± 0.55	0.62	5.16 ± 0.79	4.91 ± 0.43	0.48	4.85 ± 0.54	4.99 ± 0.29	0.63	4.80 ± 0.39	5.01 ± 0.26	0.34

Data are shown as mean ± standard deviation (SD) (n = 3). The statistical analysis was performed by Student's t-test.

Table 2. The recovery coefficients for different β -values and matrix sizes (acquisition time of 120 s and field of view of 350 mm).

Matrix size	β value	128			192			256			384		
		600	200	p-value									
Sphere diameter	6 mm	1.05 ± 0.09	1.29 ± 0.30	0.39	1.06 ± 0.07	1.39 ± 0.31	0.15	1.05 ± 0.08	1.34 ± 0.28	0.10	1.03 ± 0.09	1.33 ± 0.23	< 0.05
	8 mm	1.74 ± 0.14	3.40 ± 0.19	< 0.05	1.70 ± 0.06	3.16 ± 0.49	< 0.05	1.69 ± 0.08	3.11 ± 0.23	< 0.05	1.63 ± 0.07	2.98 ± 0.20	< 0.05
	10 mm	2.80 ± 0.18	4.25 ± 0.29	< 0.05	2.91 ± 0.11	4.86 ± 0.24	< 0.05	2.79 ± 0.12	4.26 ± 0.20	< 0.05	2.71 ± 0.12	4.36 ± 0.14	< 0.05
	20 mm	4.25 ± 0.13	4.93 ± 0.67	< 0.05	4.29 ± 0.15	4.76 ± 0.23	< 0.05	4.35 ± 0.16	4.77 ± 0.30	< 0.05	4.38 ± 0.15	4.83 ± 0.22	< 0.05
	30 mm	4.19 ± 0.24	4.96 ± 0.55	< 0.05	4.20 ± 0.21	4.91 ± 0.43	< 0.05	4.25 ± 0.19	4.99 ± 0.29	< 0.05	4.31 ± 0.15	5.01 ± 0.26	< 0.05

Data are shown as mean ± SD (n = 3). The statistical analysis was performed by Student's t-test.

Table 3. Variation in the percent background to differences in the matrix size and acquisition time.

The percent background variability (%N _{30 mm})		Acquisition time (sec)								
		60	120	180	240	300	600	900	1,800	
Matrix size	128	5.65	3.52	2.80	2.57	2.28	1.55	1.34	1.04	
	192	4.81	2.94	2.43	2.31	2.05	1.44	1.24	0.96	
	256	4.40	2.68	2.24	2.14	1.92	1.41	1.18	0.92	
	384	3.86	2.33	2.04	1.98	1.79	1.37	1.10	0.85	

the acquisition time increased.

Contrast evaluation

The contrast and the ratio of contrast to background variability for different collection times at a matrix size of 192 × 192 and a FOV of 350 mm are presented in Table 4. The contrast to background ratio of variability fluctuates from 60 s to 180 s but is stable from 180 s to 300 s. The discrepancy became ≥ 25% in the 8-mm sphere or more after the shooting time of 120 s, and the longer time, the higher contrast. The contrast was 5.9% for the 8-mm sphere and 25.6% for the 10-mm sphere in images with a matrix size of 192 × 192, FOV of 700 mm, β -value of 600, and an imaging time of 120 s. Conversely, images with a matrix size of 192 × 192, a FOV of 350 mm, a β -value of 200, and an imaging time of 120 s show high contrast of 25.5% for the 8-mm sphere and 54.3% for the 10-mm sphere.

Discussion

Using a SP-6 phantom, we investigated the optimal imaging conditions of head and neck lesion, focusing on the differences with general whole-body imaging with an FOV

of 700 mm, a matrix size of 192 × 192, and a BPL reconstruction with a β -value of 600.

Firstly, the difference between a FOV of 700 mm and 350 mm had little effect on the RC when the image was taken at 1,800 s, with a matrix size of 192 × 192 and BPL reconstruction with a β -value of 600. The 10-mm and 8-mm spheres seemed to be affected when the imaging time was set to 120 s and the matrix size was changed from 128 × 128 to 384 × 384, albeit slightly, compared to the 1,800 s imaging time. Koopman et al. (2015) and Hashimoto et al. (2018) reported that increasing the matrix size significantly improves the signal noise ratio and RC for spheres smaller than 10-mm. Conversely, Miwa et al. (2020) reported that under sufficient imaging time and considering the size of the sinogram matrix of the SiPM tubes PET/CT scanner, the detectability did not change with a pixel size of ≥ 192, similar to the present results.

Secondly, matrix size of 198 × 198 and FOV of 350 mm improved the RC by 40% for the 8-mm sphere and 28% for the 10-mm sphere using a BPL reconstruction with a β -value of 200 during image reconstruction with an acquisition time of 120 s compared to a BPL reconstruction with a β -value of 600. Generally, the larger the BPL reconstruc-

Table 4. Image quality analysis values for different acquisition times with an effective field of view of 350 mm and Bayesian penalized likelihood reconstruction method condition of a β -value of 200.

		Acquisition time (sec)							
		60	120	180	240	300	600	900	1,800
The percent contrast (%Q _p)									
Sphere diameter	6 mm	21.1	5.9	3.8	4.0	1.8	2.4	1.2	1.7
	8 mm	33.1	25.5	25.4	25.8	28.8	32.6	30.4	29.0
	10 mm	53.5	54.3	48.7	50.0	47.9	52.5	52.4	51.3
	20 mm	71.7	71.5	72.1	72.2	72.2	73.9	72.4	71.9
	30 mm	69.4	73.0	75.1	74.5	74.4	74.4	74.7	77.1
The contrast-noise ratio (Q _p /N _{30 mm})									
		Acquisition time (sec)							
		60	120	180	240	300	600	900	1,800
Sphere diameter	6 mm	4.4	2.0	1.6	1.7	0.9	1.7	1.0	1.8
	8 mm	6.9	8.7	10.4	11.2	14.0	22.6	24.6	30.2
	10 mm	11.1	18.4	20.0	21.6	23.3	36.4	42.3	53.5
	20 mm	14.9	24.3	29.6	31.2	35.2	51.3	58.5	75.0
	30 mm	14.4	24.8	30.9	32.2	36.2	51.6	60.4	80.3

tion with β -value, the stronger the smoothing (Ahn et al. 2015). Increasing the value of the BPL reconstruction with β -value reduces noise and maintains uniformity in the low-count region. Conversely, comparing the results for BPL reconstruction with β -values of 200 and 600 with a reconstructed FOV of 350 mm shows that the RC decreases with a smaller sphere for BPL reconstruction with a β -value of 600. Hence, the short imaging time resulted in a high noise component even in 8-mm and 10-mm spheres, which lowered their contrast and reduced the RC. Therefore, the intensity of the BPL reconstruction with a β -value has a greater impact on the background region and 8-mm and 10-mm spheres. In particular, a longer collection time is required to use the BPL reconstruction with a β -value of 200, and an 8-mm sphere can be delineated if background fluctuations can be suppressed and contrast can be assured.

Thirdly, the background variation was within 3.0% for an imaging time of ≥ 180 s, and the contrast was $\geq 25\%$ for the 8-mm sphere. It has been reported that the higher the tumor-to-background ratio, the smaller the lesion is depicted (Adler et al. 2017; Lindström et al. 2018; Tatsumi et al. 2021). This suggests that optimal imaging conditions and reconstruction may improve the delineation of the 8-mm sphere and detect spheres smaller than 8-mm.

Overall, we recommend that the imaging time per bed in the head and neck should be at least 180 s and the reconstruction conditions should be an FOV of 350 mm, matrix sizes of ≥ 192 , and a BPL reconstruction with a β -value of 200. This enables to detect over 70% of the images of 8-mm spheres. Such great detectability on PET/CT must be clinically useful especially in head and neck region because squamous cell carcinoma is common in this area and is

extremely FDG-avid. PET/CT findings are useful for staging and diagnosing metastasis or recurrence because they accurately identify the site of FDG accumulation in the tumor and cervical lymph nodes. Additionally, it has a higher detection rate than other modalities in the search for cancers of unknown primary detected in cervical lymph nodes (Schöder et al. 2004; Wang et al. 2006). Changes in the degree of accumulation can be used to determine the effectiveness of treatment. Kojima et al. (2022) reported that SiPM-equipped semiconductors have better imaging performance for small tongue cancer than conventional photomultiplier tube-equipped PET/CT systems. Taking advantage of the feature that the imaging time per bed can be varied in PET/CT examinations during whole-body imaging, we clarified the effects of differences in imaging time, reconstructed FOV, and matrix size in the head and neck region on the lesion delineation performance.

In conclusion, the imaging time per bed in the head and neck should be at least 180 s, and the reconstruction conditions should be an FOV of 350 mm, matrix sizes of ≥ 192 , and a BPL reconstruction with a β -value of 200. This enables to detect over 70% of the images of 8-mm spheres.

Acknowledgments

The authors thank the Nuclear Medicine Laboratory staff of the Division of Radiology, the Department of Medical Technology, and Tohoku University Hospital for their valuable support.

Conflict of Interest

The authors declare no conflict of interest.

References

- Adler, S., Seidel, J., Choyke, P., Knopp, M.V., Binzel, K., Zhang, J., Barker, C., Conant, S. & Maass-Moreno, R. (2017) Minimum lesion detectability as a measure of PET system performance. *EJNMMI Phys.*, **4**, 13.
- Ahn, S., Ross, S.G., Asma, E., Miao, J., Jin, X., Cheng, L., Wollenweber, S.D. & Manjeshwar, R.M. (2015) Quantitative comparison of OSEM and penalized likelihood image reconstruction using relative difference penalties for clinical PET. *Phys. Med. Biol.*, **60**, 5733-5751.
- Beyer, T., Townsend, D.W., Brun, T., Kinahan, P.E., Charron, M., Roddy, R., Jerin, J., Young, J., Byars, L. & Nutt, R. (2000) A combined PET/CT scanner for clinical oncology. *J. Nucl. Med.*, **41**, 1369-1379.
- Chicheportiche, A., Marciano, R. & Orevi, M. (2020) Comparison of NEMA characterizations for Discovery MI and Discovery MI-DR TOF PET/CT systems at different sites and with other commercial PET/CT systems. *EJNMMI Phys.*, **7**, 4.
- Daisaki, H., Kitajima, K., Nakajo, M., Watabe, T., Ito, K., Sakamoto, F., Nakahara, T., Ishibashi, M. & Torihara, A. (2021) Usefulness of semi-automatic harmonization strategy of standardized uptake values for multicenter PET studies. *Sci. Rep.*, **11**, 8517.
- Fletcher, J.W., Djulbegovic, B., Soares, H.P., Siegel, B.A., Lowe, V.J., Lyman, G.H., Coleman, R.E., Wahl, R., Paschold, J.C., Avril, N., Einhorn, L.H., Suh, W.W., Samson, D., Delbeke, D., Gorman, M., et al. (2008) Recommendations on the use of 18F-FDG PET in oncology. *J. Nucl. Med.*, **49**, 480-508.
- Fukukita, H., Suzuki, K., Matsumoto, K., Terauchi, T., Daisaki, H., Ikari, Y., Shimada, N. & Senda, M. (2014) Japanese guideline for the oncology FDG-PET/CT data acquisition protocol: synopsis of Version 2.0. *Ann. Nucl. Med.*, **28**, 693-705.
- Hashimoto, N., Morita, K., Tsutsui, Y., Himuro, K., Baba, S. & Sasaki, M. (2018) Time-of-flight information improved the detectability of subcentimeter spheres using a clinical PET/CT scanner. *J. Nucl. Med. Technol.*, **46**, 268-273.
- Ishii, K., Hanaoka, K., Watanabe, S., Morimoto-Ishikawa, D., Yamada, T., Kaida, H., Yamakawa, Y., Minagawa, S., Takenouchi, S., Ohtani, A. & Mizuta, T. (2023) High-resolution silicon photomultiplier time-of-flight dedicated head PET system for clinical brain studies. *J. Nucl. Med.*, **64**, 153-158.
- Kojima, I., Takanami, K., Ogawa, T., Ishikawa, K., Morishita, Y., Ishii, R., Ohkoshi, A., Nakanome, A., Odagiri, H. & Iikubo, M. (2022) High diagnostic accuracy for lymph node metastasis of oral squamous cell carcinoma using PET/CT with a silicon photomultiplier. *Oral Radiol.*, **38**, 540-549.
- Koopman, D., van Dalen, J.A., Lagerweij, M.C., Arkies, H., de Boer, J., Oostdijk, A.H., Slump, C.H. & Jager, P.L. (2015) Improving the detection of small lesions using a state-of-the-art time-of-flight PET/CT system and small-voxel reconstructions. *J. Nucl. Med. Technol.*, **43**, 21-27.
- Kurita, Y., Ichikawa, Y., Nakanishi, T., Tomita, Y., Hasegawa, D., Murashima, S., Hirano, T. & Sakuma, H. (2020) The value of Bayesian penalized likelihood reconstruction for improving lesion conspicuity of malignant lung tumors on ¹⁸F-FDG PET/CT: comparison with ordered subset expectation maximization reconstruction incorporating time-of-flight model and point spread function correction. *Ann. Nucl. Med.*, **34**, 272-279.
- Lindström, E., Oddstig, J., Danfors, T., Jogi, J., Hansson, O. & Lubberink, M. (2020) Image reconstruction methods affect software-aided assessment of pathologies of [¹⁸F]flutemetamol and [¹⁸F]FDG brain-PET examinations in patients with neurodegenerative diseases. *Neuroimage Clin.*, **28**, 102386.
- Lindström, E., Sundin, A., Trampal, C., Lindsjö, L., Ilan, E., Danfors, T., Antoni, G., Sorensen, J. & Lubberink, M. (2018) Evaluation of penalized-likelihood estimation reconstruction on a digital time-of-flight PET/CT scanner for ¹⁸F-FDG whole-body examinations. *J. Nucl. Med.*, **59**, 1152-1158.
- Miwa, K., Wagatsuma, K., Nemoto, R., Masubuchi, M., Kamitaka, Y., Yamao, T., Hiratsuka, S., Yamaguchi, M., Yoshii, T., Kobayashi, R., Miyaji, N. & Ishii, K. (2020) Detection of sub-centimeter lesions using digital TOF-PET/CT system combined with Bayesian penalized likelihood reconstruction algorithm. *Ann. Nucl. Med.*, **34**, 762-771.
- Schöder, H., Yeung, H.W., Gonen, M., Kraus, D. & Larson, S.M. (2004) Head and neck cancer: clinical usefulness and accuracy of PET/CT image fusion. *Radiology*, **231**, 65-72.
- Tateishi, U., Daisaki, H., Tsuchiya, J., Kojima, Y., Takino, K., Shimada, N. & Yokoyama, K. (2021) Image quality and quantification accuracy dependence on patient body mass in ⁸⁹Zr PET/CT imaging. *EJNMMI Phys.*, **8**, 72.
- Tatsumi, M., Soeda, F., Kamiya, T., Ueda, J., Katayama, D., Matsunaga, K., Watabe, T., Kato, H. & Tomiyama, N. (2021) Effects of new Bayesian penalized likelihood reconstruction algorithm on visualization and quantification of upper abdominal malignant tumors in clinical FDG PET/CT examinations. *Front. Oncol.*, **11**, 707023.
- Teoh, E.J., McGowan, D.R., Macpherson, R.E., Bradley, K.M. & Gleeson, F.V. (2015) Phantom and clinical evaluation of the Bayesian penalized likelihood reconstruction algorithm Q. Clear on an LYSO PET/CT system. *J. Nucl. Med.*, **56**, 1447-1452.
- Wagatsuma, K., Sakata, M., Ishibashi, K., Hirayama, A., Kawakami, H., Miwa, K., Suzuki, Y. & Ishii, K. (2020) Direct comparison of brain [¹⁸F]FDG images acquired by SiPM-based and PMT-based PET/CT: phantom and clinical studies. *EJNMMI Phys.*, **7**, 70.
- Wang, D., Schultz, C.J., Jursinic, P.A., Bialkowski, M., Zhu, X.R., Brown, W.D., Rand, S.D., Michel, M.A., Campbell, B.H., Wong, S., Li, X.A. & Wilson, J.F. (2006) Initial experience of FDG-PET/CT guided IMRT of head-and-neck carcinoma. *Int. J. Radiat. Oncol. Biol. Phys.*, **65**, 143-151.